ADVANCED FUNCTIONAL MATERIALS
www.afm-journal.de

Turning on Selective H_2S Gas Sensing Activity in Ternary Nickel Tungstate Strongly Correlated Electron System Through Sub-Gap Band Manipulation

Seung Yong Lee, Ha Eun Choa, Seung Joon Choi, Chul Oh Park, Gi Hyun Park, June Won Suh, Si Hoon Jeong, Yunseong Ji, Changhyun Jin, Jeong Yun Hwang, Inseo Kim, Jihye Park, Joonho Bang, Myung Sik Choi, Hyo-Jick Choi, Dong Won Chun, Kimoon Lee, Wooyoung Lee,* and Kyu Hyoung Lee**

Sensing the precise concentration of chemicals within a complex atmosphere stands as a critical technology with far-reaching implications in environmental, agricultural, and medical domains. While sensitivity limits are pushed down to the ppb levels through diverse material tuning approaches, ensuring robust selectivity for targeted analyte gases remains a challenge due to the absence of effective methodologies. Here, a band structure modulation is presented in the selective detection of H_2S utilizing $NiWO_4$-based compound, achieved through strategically manipulating sub-gap states. The approach involves tailoring the sub-gap within $NiWO_4$ by employing point defect engineering mechanisms of Cu substitutional and Li interstitial doping. Unlike the featureless pristine and Cu-doped $NiWO_4$, Li/Cu-co-doped $NiWO_4$ exhibits a sensing response to H_2S gas, exhibiting an approximately six-fold increase in sensitivity. Through density functional theory calculations and Mott–Schottky analysis, it is unveiled that this high sensitivity and selectivity toward H_2S stem from the generation and positioning of Cu *d*-orbital-derived sub-gap states, matching the reduction potential of H_2S, which is triggered in the presence of substitutional Cu and interstitial Li. This result suggests a novel strategy for customizing sensing materials based on the reduction potential of analyte gases.

1. Introduction

Accurate monitoring of analyte gas concentrations in mixed atmospheres has become increasingly crucial due to the expansion of industries employing a diverse range of chemicals. Among solid-state sensors, metal oxides (MO) have garnered significant attention owing to their simplicity, cost-effectiveness, high stability, and sensitivity.[1–6] The fundamental principle of gas sensing involves the association and dissociation of oxygen with gases at the surface of MO, leading to variations in electrical resistance, commonly known as gas response. For instance, dissociated oxygen atoms within oxygen vacancy sites lose electrons from the MO, resulting in decreased electron carrier density and increased electrical resistance (for *n*-type gas sensors). Conversely, reducing gases interact with the MO surface oxygen, donating electrons and causing resistance to decrease (*p*-type gas

S. Y. Lee, H. E. Choa, S. J. Choi, C. O. Park, G. H. Park, J. W. Suh, S. H. Jeong, Y. Ji, C. Jin, J. Y. Hwang, W. Lee, K. H. Lee
Department of Materials Science and Engineering
Yonsei University
Seoul 03722, Republic of Korea
E-mail: wooyoung@yonsei.ac.kr; khlee2018@yonsei.ac.kr

I. Kim, K. Lee
Department of Physics
Kunsan National University
Gunsan 54150, Republic of Korea
E-mail: kimoon.lee@kunsan.ac.kr

The ORCID identification number(s) for the author(s) of this article can be found under https://doi.org/10.1002/adfm.202425477

DOI: 10.1002/adfm.202425477

J. Park, J. Bang
Department of Materials Engineering and Convergence Technology
Gyeongsang National University
Jinju 52828, Republic of Korea

J. Bang
School of Materials Science and Engineering
Gyeongsang National University
Jinju 52828, South Korea

M. S. Choi
School of Nano & Materials Science and Engineering
Kyungpook National University
Sangju 37224, Republic of Korea

H.-J. Choi
Department of Chemical and Materials Engineering
University of Alberta
Edmonton, AB T6G 1H9, Canada

D. W. Chun
Department of Materials Science and Engineering
Pohang University of Science and Technology (POSTECH)
Pohang 37673, Republic of Korea

sensors).[7–9] Despite these advantages, the relatively poor selectivity of MO gas sensors impedes their commercialization, as they exhibit unintentional responses to untargeted gas species in mixed environments. While numerous approaches aim to enhance selectivity in MO gas sensors, most methodologies necessitate external stimuli or additional fabrications such as temperature modulation or array combinations. Thus, there is a pressing need for a more intrinsic approach to materials tuning itself.

Considering that charge transfer is the key mechanism governing gas sensing behavior, tailoring a chemical barrier to facilitate charge transfer between the analyte gas and MO surface emerges as a fundamental strategy for developing exclusive gas-selective materials.[4,5] Similarly, in the selection of candidate catalyst materials, ensuring alignment between the band structure of the catalyst and the reduction potential of the target chemical is critical for optimizing catalytic reaction efficiency and promoting enhanced charge transfer.[10–18] Inspired by the mechanisms governing selective catalyst action, electronic band engineering within MO materials to align with the reduction potential of the analyte gas holds immense potential for achieving unparalleled gas selectivity. Strongly correlated oxide systems represent promising candidates for manipulating band structures due to the strong Coulombic potential among *d*-band electrons.[19–27] Through modulation of the degree of correlation, significant alterations in physical states, such as metal-insulator transitions and the emergence of superconductivity, can be attained.[19–22] Leveraging the Hubbard band in strongly correlated oxides, influenced by U/t (where U is the Coulombic potential and t is the transfer integral between 3*d* electrons), offers a pathway to finely tune chemical activity via band engineering in accordance with the reduction potential of the analyte gas.

Here, we tailor the strongly correlated oxide $NiWO_4$ by co-doping it with Cu and Li at distinct sites (Cu substitutes the Ni site, while Li occupies interstitial space) within its crystal structure. Each dopant serves different roles in electrical and chemical activation. We created a band structure with the potential to form a sub-gap between CBM (Conduction band minimum) and VBM (valence band maximum) by Cu substitution, and the sub-gap level can be tuned by the additional doping of Li. This band structure manipulation resulted in exclusive H_2S sensing performance with over 6-times more responsivity than other gases. This work proposes a compositional tuning approach to evoke highly selective H_2S sensitivity from featureless MO insulators by band structure modulation.

2. Results and Discussion

2.1. Structural Characterization of $NiWO_4$-Based Compounds

Compacted bulks of $NiWO_4$, $Cu_{0.25}Ni_{0.75}WO_4$ (Cu-$NiWO_4$), and $Li_{0.10}Cu_{0.25}Ni_{0.75}WO_4$ (Li/Cu-$NiWO_4$) for H_2S gas sensing were prepared by a solid-state reaction (Figure S1, Supporting Information) and a subsequent CIP (cold isostatic pressing) process. The synthesized powders exhibited an average size of less than 5 µm, with a granular aggregate shape, as confirmed both by scanning electron microscopy (SEM) images (**Figure 1a–c**) and BET results (Figure S2, Supporting Information). The darker color of Cu-$NiWO_4$ and Li/Cu-$NiWO_4$ compared to pristine $NiWO_4$, as shown in the inset photo of the SEM results, implies a difference in carrier density and conductivity in the doped $NiWO_4$ samples. The cationic element mapping results obtained from energy dispersive X-ray spectrometer (EDS) and time-of-flight secondary ion mass spectrometry (TOF-SIMS) measurements (Figure S3, Supporting Information) indicated that the cationic elements of Cu, Ni, and Li were homogeneously dispersed in the synthesized particles without segregation. The inductively coupled plasma-mass spectrometry (ICP-MS) results in Table S1 (Supporting Information) showed a similar composition ratio of cations between the nominal and actual content in the samples. The crystal structure of Li/Cu-$NiWO_4$ was illustrated in Figure 1d as determined by Rietveld refinement analysis of powder X-ray diffraction (PXRD) patterns in Figure S4 (Supporting Information) (Detailed fitting parameters are listed in Table S2, Supporting Information). The analyzed crystal structure of Li/Cu-$NiWO_4$ indicated a monoclinic structure with P2/C space group symmetry, composed of two octahedral sublattices ([NiO_6] and [WO_6]) that shared oxygen atoms. Each octahedral structure exhibited a cation-oxygen bonding length of ≈2 Å. On the other hand, the distance between the nearest [NiO_6] octahedral sublattices was ≈3 Å, which is relatively longer than that between cation and oxygen, suggesting the existence of free space between the octahedral structures. The Rietveld analysis results, along with the reported crystal structure of *n*-type MO semiconductor $CuWO_4$,[28,29,30] confirmed the P2/C space group symmetry and the substitutional dopant. As shown in Figure 1e, the unit cell volume of $NiWO_4$ was increased by Cu addition, while slightly decreased by Li addition.

2.2. Vibrational Study of Cu, Li-Doped $NiWO_4$ Compounds

To identify the site of Li atoms in $NiWO_4$, Raman spectroscopy was performed on $NiWO_4$, Cu-$NiWO_4$, and Li/Cu-$NiWO_4$ samples. Figure 1f depicts the characteristic vibration modes of [NiO_6] (near 360 cm^{-1}) and [WO_6] (near 700 and 890 cm^{-1}) in the wolframite structure.[31,32] The inset of Figure 1f shows the redshift of the [NiO_6] vibration mode, while there are negligible shifts in both the symmetric and asymmetric vibration modes of the [WO_6] octahedral structure. Accompanied by structural characterization results from Rietveld analysis, the redshift of the [NiO_6] vibration peak from $NiWO_4$ to Cu-$NiWO_4$ indicates the successful Cu substitution mainly on the Ni-site rather than W-site, as increasing the lattice parameters.[27] It is worthwhile to note that Li/Cu-$NiWO_4$ exhibits an additional redshift only in the [NiO_6] vibrational mode, while there is negligible structural distortion compared to that from Cu-$NiWO_4$. Given that the interstitial Li position affects the nearest atomic vibrational mode,[33] it suggests that Li occupies not on the substitutional site but the interstitial one near the [CuO_6]/[NiO_6] octahedra. DFT calculation results (Figure S5, Supporting Information; the strongly

D. W. Chun
nstitute for Convergence Research and Education in Advanced Technology
Yonsei University, Republic of Korea

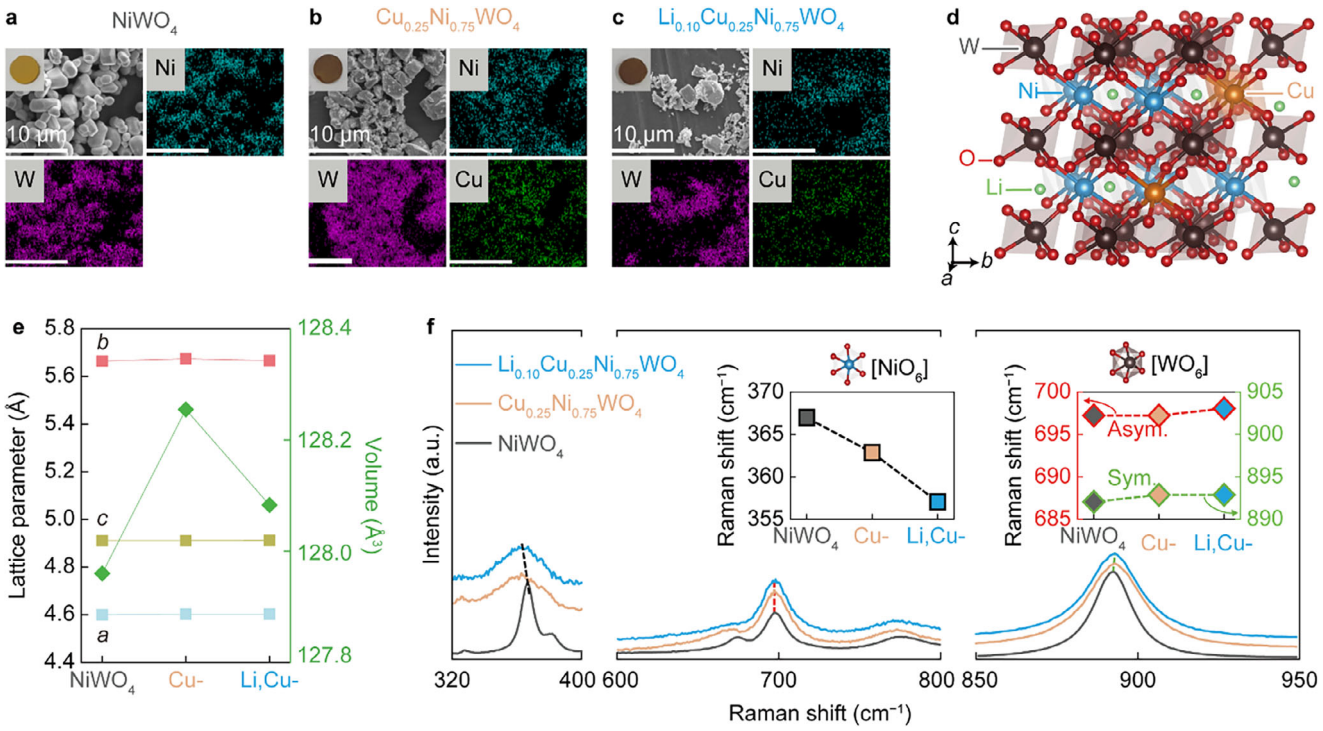

Figure 1. Structure analysis of the different roles of the Cu and Li dopants in $NiWO_4$. a–c) SEM and EDS mapping results of each sample. Samples of photos are displayed on the inset. a) $NiWO_4$, b) $Cu_{0.25}Ni_{0.75}WO_4$, and c) $Li_{0.10}Cu_{0.25}Ni_{0.75}WO_4$. d) Schematically illustrated crystal structure of $Li_{0.10}Cu_{0.25}Ni_{0.75}WO_4$. Cu is in the substitutional site of Ni, and Li is located in the free space of $NiWO_4$. e) Plots of lattice parameters derived from Rietveld refinement of each sample (Figure S5 and Table S2, Supporting Information). f) Raman spectra from $NiWO_4$, $Cu_{0.25}Ni_{0.75}WO_4$, and $Li_{0.10}Cu_{0.25}Ni_{0.75}WO_4$ samples. The characteristic peak positions for Ni-O and W-O vibrational modes are plotted in the inset.

correlated electron system behavior of $NiWO_4$ described in U_{eff} considered PDOS and magnetic properties in Figures S6, S7, Supporting Information, respectively) support well such a feature of the Li in the interstitial site. Comparing the total energies from $Cu_{0.25}Ni_{0.75}WO_4$ structures with various Li defect sites, the most stable Li site was the empty space between the $[CuO_6]/[NiO_6]$ octahedra sublattices. This firmly reveals that the Li dopant prefers to occupy an interstitial site near Ni/Cu rather than a substitutional one in parent $NiWO_4$.

2.3. Chemical and Electrical Analysis in Cu, Li-Doped $NiWO_4$ Compounds

XPS data in **Figure** 2a–c and S8 (Supporting Information) represent the chemical states of cations in the Ni 2*p* and W 4*f* core level spectra between $NiWO_4$ and Cu-$NiWO_4$, indicating that Cu substitution does not influence the chemical states of cations in $NiWO_4$. Contrary to Cu substitution, a higher ratio of Ni^{2+}, W^{5+}, and Cu^{+} valence states than Ni^{3+}, W^{6+}, and Cu^{2+} were observed by Li introduction. This strongly supports that the interstitial Li dopant acts as an electron donor site in the $NiWO_4$ matrix, resulting in less positively charged cationic valence states. Such changes in chemical states with Cu and Li doping affect the electrical properties of $NiWO_4$. Figure 2d–f and Figure S9 (Supporting Information) present the AC electrical resistivity (ρ_{AC}) measurement results at different frequencies up to 330 °C for $NiWO_4$, Cu-$NiWO_4$, and Li/Cu-$NiWO_4$. The ρ_{AC} value decreases drastically, by a factor of 100, upon Cu substitution, while it remains nearly constant following the introduction of interstitial Li. By fitting the temperature (T) dependence of ρ_{AC} curves, we extract the activation energy for polaron hopping (E_a). The E_a value is significantly reduced by Cu substitution compared to pristine $NiWO_4$, whereas it maintains unchanged for Li/Cu-$NiWO_4$ relative to Cu-$NiWO_4$. Since the structural parameters are more strongly affected by Cu substitution by the addition of interstitial Li, this suggests that the reduction in ρ_{AC} is originated not by carrier doping but primarily by enhanced polaron hopping efficiency, a phenomenon also observed in other Ni-based transition metal oxides.[27] Supported by XPS results, the findings indicate that Li/Cu-$NiWO_4$ exhibits improved electrical conductivity due to the synergetic effects of Cu-induced efficient carrier hopping between polaron sites and chemically frustrated states created by extra electron donation through Li interstitial defects.

2.4. Activating H_2S Gas Sensing Properties in Cu, Li-Doped $NiWO_4$

The improved electron conductivity as well as frustrated chemical states of Li/Cu-$NiWO_4$ exhibit exclusive H_2S gas sensing performance compared to $Cu_{0.25}Ni_{0.75}WO_4$ and $NiWO_4$. The chemical sensing measurement was performed using a two-probe setup on pelletized samples in a gas-sensing system, as depicted in **Figure** 3a and S10 (Supporting Information). The representative chemical sensing results under H_2S gas exposure are

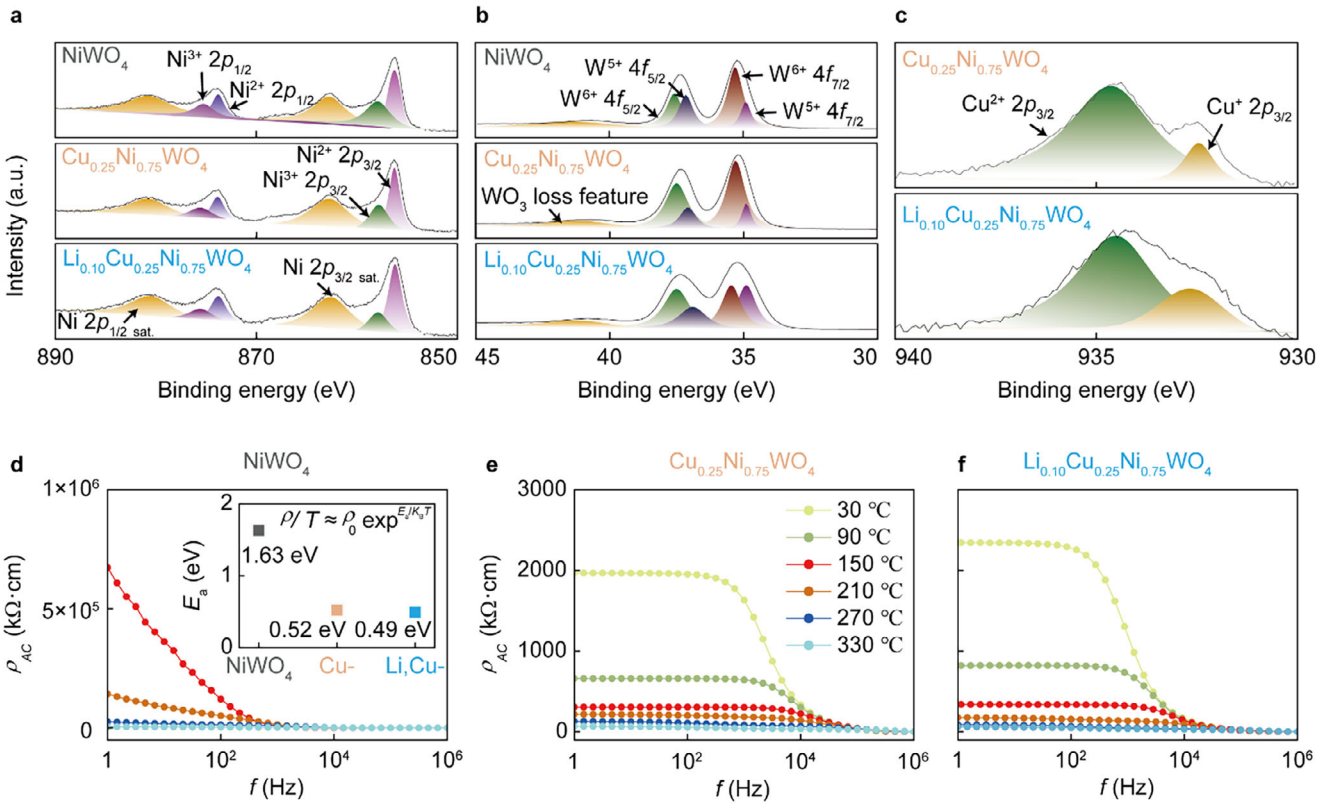

Figure 2. a–c) XPS results of $NiWO_4$, Cu-$NiWO_4$, and Li/Cu-$NiWO_4$ samples with different cation regions as a) Ni 2p orbital, b) W 4f orbital, and c) Cu 2p orbital. d–f) Frequency-dependent AC resistivity values of d) $NiWO_4$, e) Cu-$NiWO_4$, and f) Li/Cu-$NiWO_4$ until 330 °C. Calculated activation energy values are shown in the inset of (d).

shown in Figure 3b. Li/Cu-$NiWO_4$ exhibits a much higher response to H_2S gas up to ≈6 R_g/R_a at 300 °C, surpassing those of pristine $NiWO_4$ and Cu-$NiWO_4$. The inset of Figure 3b shows a decrease in resistance when exposed to H_2S gas, indicating an *n*-type nature for Cu-$NiWO_4$ and Li/Cu-doped $NiWO_4$, in contrast to the *p*-type behavior from intrinsic $NiWO_4$ as consistent with other reports[4,5,9] (All sensor types under different gases are shown in Figure S11 (Supporting Information) and the gas response direction depending on the analyte gases are displayed in Figure S12, Supporting Information).

To investigate the gas selectivity of Li/Cu-$NiWO_4$, we examined its response to 11 different gases, including various oxidizing (NO_2 and SO_2), reducing (H_2S, NH_3, H_2), and volatile organic gases (VOCs: C_3H_6O, C_6H_6, C_7H_8, CO, P-xylene, and C_2H_5OH) at the same gas concentration (10 ppm) and measuring *T* (300 °C). As clearly shown in Figure 3c, only Li/Cu-$NiWO_4$ exhibits a higher H_2S gas response and selectivity compared to $NiWO_4$ and Cu-$NiWO_4$. Furthermore, we performed additional gas sensing measurements using different densities of Li in $Cu_{0.25}Ni_{0.75}WO_4$ (noted as $Li_xCu_{0.25}Ni_{0.75}WO_4$, $x = 0.03$, 0.1, 0.2) under 10 ppm of each analyte gases at 300 °C as shown in Figure S13 (Supporting Information). The plot of the gas selectivity of $Li_xCu_{0.25}Ni_{0.75}WO_4$ is displayed in Figure 3d, which indicates the higher H_2S selectivity on the $Li_{0.10}Cu_{0.25}Ni_{0.75}WO_4$ than the other Li concentration. To detail an understanding of the underlying gas sensing mechanism of higher H_2S selectivity on $Li_{0.10}Cu_{0.25}Ni_{0.75}WO_4$, we measured H_2-TPR up to 800 °C (Figure S14, Supporting Information), which shows the reduction temperature under H_2 environment. The weak reduction ranges from 300 to 400 °C is related to proper gas sensing temperature as displayed in Figure 3e. Interestingly, H_2S gas sensing performance of $Li_{0.10}Cu_{0.25}Ni_{0.75}WO_4$ gradually increases with increasing temperature, and such a gas responsibility of endures well even after 3 months as shown in the inset of Figure 3e. The H_2S selectivity strongly suggests that the gas sensing mechanism could be distinct in $Li_{0.10}Cu_{0.25}Ni_{0.75}WO_4$ surface from the conventional MO surface involving oxygen association and dissociation process.[4,5,9]

2.5. Study on the Origin of H_2S Gas Sensing Mechanism in Li,Cu-$NiWO_4$

To analyze the change in the electronic structure of $NiWO_4$, Cu-$NiWO_4$, and Li/Cu-$NiWO_4$, we performed DFT calculations. To account for the correlation in transition metal *d*-electrons, we considered the Coulomb interaction (*U*) and exchange (*J*) parameters, with an effective Coulomb repulsion value ($U_{eff} = U - J$) of 5.3 eV for the Ni 3*d* and Cu 3*d* orbitals.[19] As observed in **Figure 4a–c**, the energetic distance between the VBM and CBM slightly decreases with the introduction of dopants, indicating insignificant band gap (E_g) reduction by doping of Cu and Li. Comparing pristine $NiWO_4$, the sub-gap state mainly consisting of Cu *d*-orbitals appears by Cu substitution at Ni-site (Figure 4b).

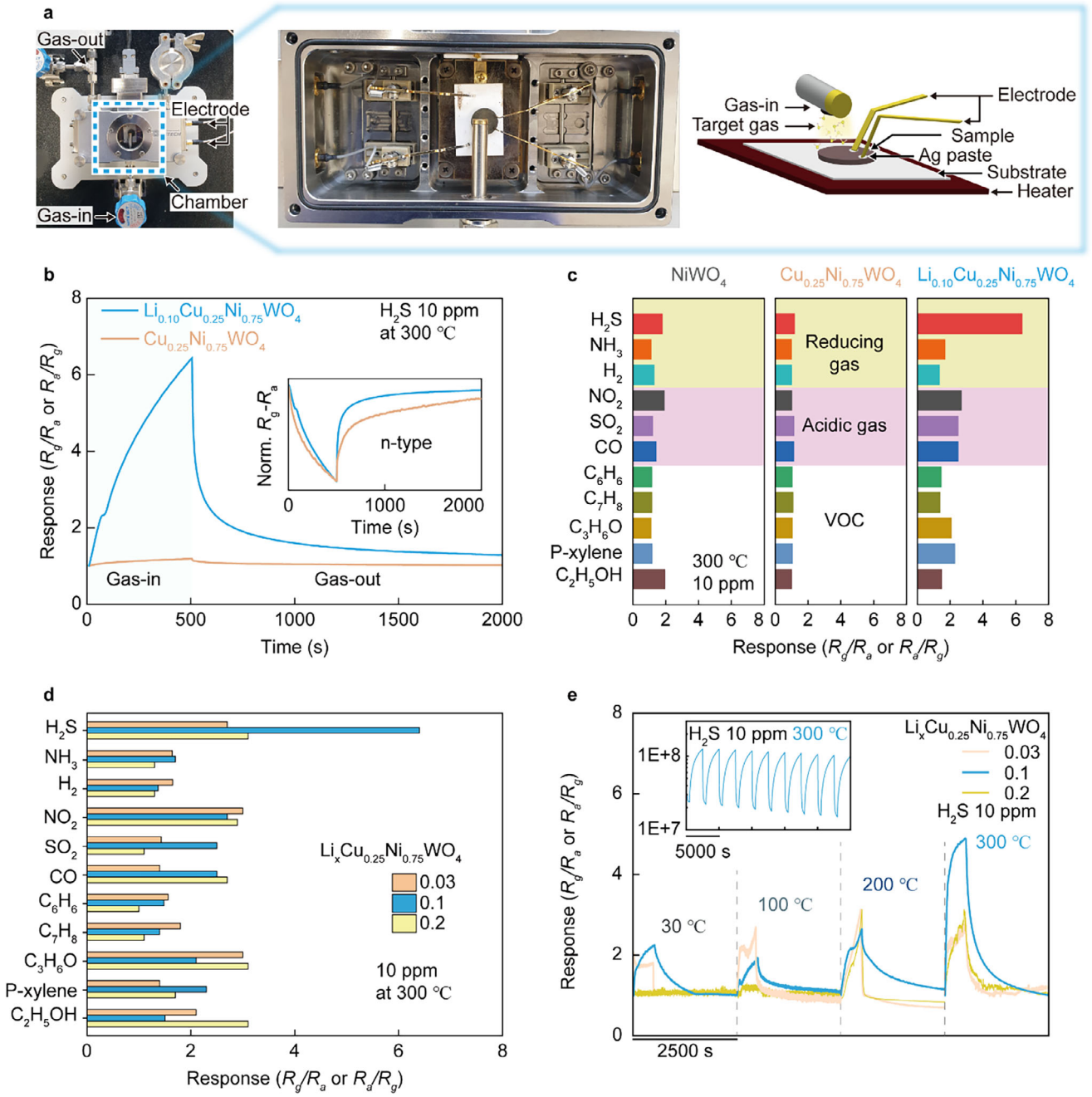

Figure 3. a) Measuring system of sensing properties. b) Response (R_g/R_a or R_a/R_g) of $Cu_{0.25}Ni_{0.75}WO_4$ and $Li_{0.10}Cu_{0.25}Ni_{0.75}WO_4$ for H_2S gas (10 ppm). Inset is $R_g - R_a$ plot for confirming the conduction type. c) Gas selectivity under various gases derived from Figures S11, S12 (Supporting Information). d) Gas selectivity of $Li_xCu_{0.25}Ni_{0.75}WO_4$ depending on the interstitial Li concentration. e) Comparing response under different temperatures. Inset shows the change in response in long-term stability.

It should be noted that such a sub-gap level position is relatively closer to the CBM rather than the VBM, suggesting that electron transition between the sub-gap state and CBM is more probable than that between the sub-gap state and VBM. This sub-gap state splits into two distinct levels with additional Li introduction as shown in Figure 4c, probably due to the encouraged Coulombic repulsion in the Cu *d*-band by electron addition, as experimentally observed from XPS results with increased Cu^+ state (See Figure 2c, Supporting Information). From the results showing that the gas sensing properties are most remarkable in Li/Cu-$NiWO_4$, it strongly suggest that these split sub-gap states play a key role in highly responsive and selective H_2S gas sensing. To reveal the relationship between the electronic states and gas sensing properties, we performed Mott-Schottky measurements to derive the reduction potential of $NiWO_4$, Cu-$NiWO_4$, and Cu/Li-$NiWO_4$ (Figure 4d; Figure S15, Supporting Information). The flat

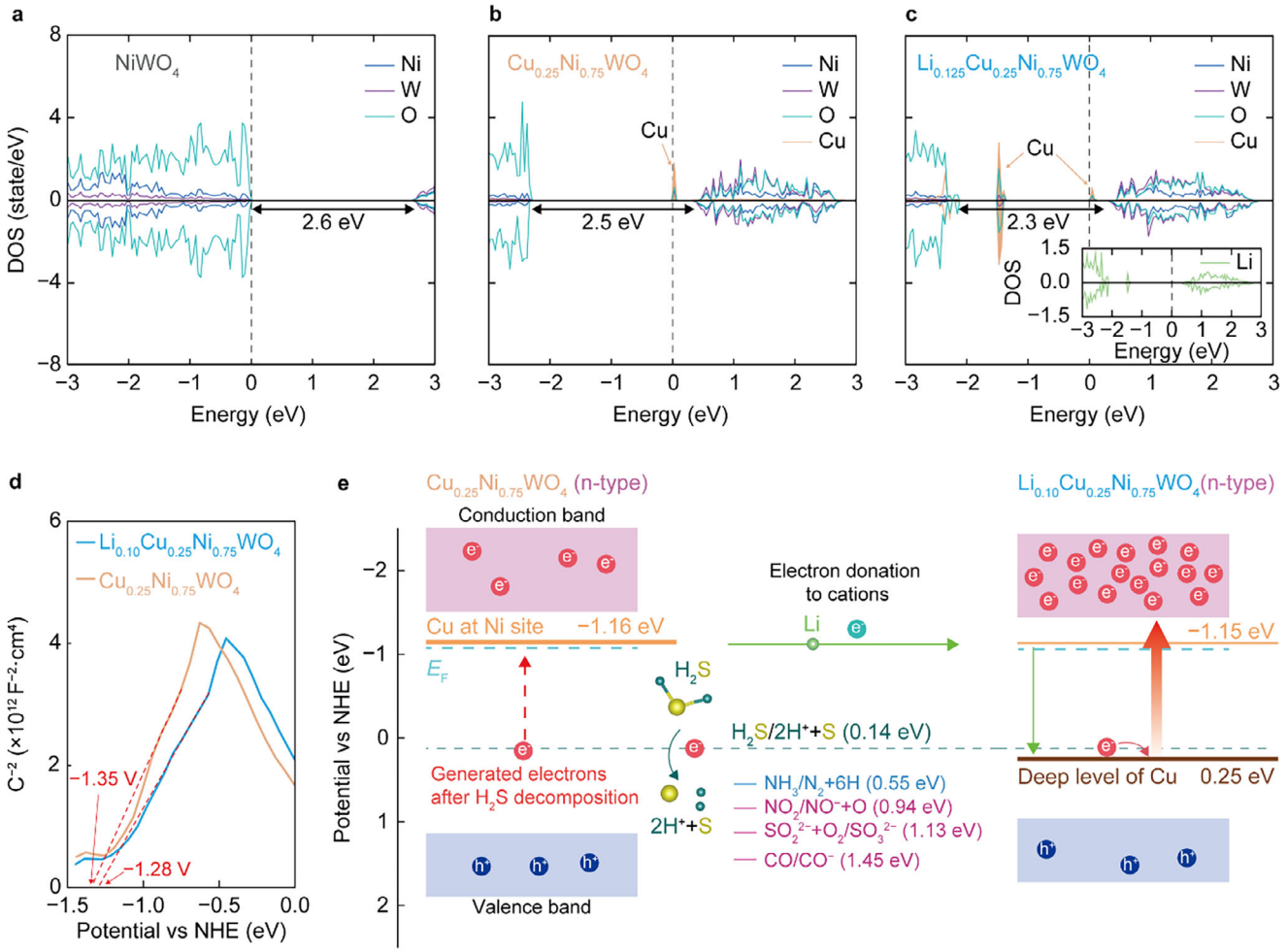

Figure 4. Mechanism of the emergence of H_2S sensing in $NiWO_4$ by modulating band structure and reduction potential using the different roles of Li/Cu-$NiWO_4$. PDOS results of a) $NiWO_4$, b) $Cu_{0.25}Ni_{0.75}WO_4$, and c) $Li_{0.125}Cu_{0.25}Ni_{0.75}WO_4$, respectively. The Li-PDOS is in the Figure 4c inset. d) Mott–Schottky results of $Cu_{0.25}Ni_{0.75}WO_4$ and $Li_{0.10}Cu_{0.25}Ni_{0.75}WO_4$. The full range results are in Figure S15 (Supporting Information). e) Reduction potentials of oxidizing and reducing gas and schematic band structures compared with H_2S reduction potential. The change of resistance by the generation of depletion layer particles under H_2S is depicted in the downside of the band structure.

band potential of all compositions with respect to the normal hydrogen electrode (NHE) derived from Mott-Schottky results demonstrates the VBM level of 1.61 V in *p*-type $NiWO_4$, while CBM levels of −1.35 and −1.28 V in *n*-type Cu-$NiWO_4$ and Li/Cu-$NiWO_4$, respectively. Based on these obtained reduction potential values, the relative potential level between various gases and electronic band levels can be illustrated as shown in Figure 4e. The H_2S gas reduction potential matches well only with the lower sub-gap level from Li/Cu-$NiWO_4$ with a very small difference of 0.11 eV. It means that the electrons can easily transfer between the lower sub-gap states of Li/Cu-$NiWO_4$ and H_2S gas, thus evidently resulting in strong responsivity as well as high selectivity, in particular to H_2S gas for Li/Cu-$NiWO_4$. Because the resistance changes in gas sensing exhibit *n*-type behavior, the electron transfer route from H_2S gas to CBM can be deduced to mediate both lower and upper sub-gap states in Li/Cu-$NiWO_4$. Considering that such a direct charge transfer mechanism in gas sensing is rather similar to simple metals and/or reactive chalcogenides than traditional MOs comprising with relatively irreversible oxygen association and dissociation process,[9,34] it is advantageous for stable and reliable gas sensing performance, as demonstrated in the long-term durability test in Figure 3e. In conclusion, the activation of exceptional gas sensing performance with high responsivity, selectivity, and reliability in Li/Cu-$NiWO_4$, distinct from other oxides, originates from the *d*-band-derived sub-gap manipulation that can be precisely controlled by electron correlation control, thus promoting the charge transfer efficiency to the target gas reduction potential.

3. Conclusion

We introduce a definitive band engineering strategy based on sub-gap state formation in metal oxides to achieve selective gas sensing performance. In the strongly correlated oxide $NiWO_4$, which has a large band gap of ≈2.6 eV, Cu substitution at Ni-sites introduces sub-gap states primarily composed of Cu *d*-orbitals near the CBM. Additional interstitial Li doping further tunes the energy levels of these sub-gap states, optimizing the chemical

potential and enhancing H_2S gas sensitivity. DFT calculations and Mott–Schottky measurements reveal that the enhanced H_2S sensitivity of $Li_{0.10}Cu_{0.25}Ni_{0.75}WO_4$ arises from appropriately leveled sub-gap states that align with the H_2S reduction potential. These states, dominated by *d*-band Cu-impurity contributions, can be precisely manipulated through electronic correlations. Our findings offer a new pathway for targeted gas sensing by modulating the band structure, even in non-electrochemically active materials. This approach introduces a novel and general defect engineering framework for enhancing the electro-catalytic activity of strongly correlated materials.

4. Experimental Section

Materials and Methods—Synthesis of Sensing Materials and Preparation of Sensor: The $NiWO_4$, $Cu_{0.25}Ni_{0.75}WO_4$, $Li_{0.10}Cu_{0.25}Ni_{0.75}WO_4$ powders were synthesized by solid-state reaction as schematically depicted in Figure S1 (Supporting Information). The stoichiometric mixture of CuO, Li_2CO_3, NiO, and WO_3 powders was calcined at 900 °C for 12 h in an alumina crucible. The obtained powders were pulverized and mixed using an alumina mortar, then heat-treated at 1100 °C for 12 h to fabricate a single-phase material. Disc-type samples with a diameter of 10 mm and a thickness of 1 mm were fabricated by a combination of uniaxial press and CIP under 300 MPa for 10 min. To prepare the sensing device, the silver paste was coated on two separate spots on the CIPed pellet surface and contacted with electronic probes depicted in Figure S10 (Supporting Information).

Measurement of Physical and Chemical Characteristics: The structure analysis of sensing materials was conducted using a powder X-ray diffractometer (XRD, Rigaku Smartlab, Japan). The gathered XRD spectra were recorded in the angular range (2θ) of 10°– 80° using $K\alpha 1$ radiation of copper (λ = 1.54059 Å) and the crystal structure was refined using GSAS2. The measurement of polarity and dipole vibration modes was performed by Raman spectroscopy (LabRam Aramis, Horriba Jobin Yvon, Japan) and Fourier-transform infrared spectroscopy (FT-IR spectroscopy, Vertex 70, Bruker, United States), respectively. The elemental oxidation states were analyzed by X-ray photoelectron spectroscopy (XPS, K-alpha, Thermo Fisher Scientific, United States). Microstructure and morphological analyses were conducted by using scanning electron microscopy (SEM, JEOL JSM-7001F, Japan) and BET (Brunauer–Emmett–Teller) system (Autosorb-iQ 2ST/M.P, system Quantachrome, United States).

The qualitative and quantitative analysis was performed using energy-dispersive X-ray spectroscopy (EDS) for heavy cation mapping and time-of-flight secondary ion mass spectroscopy (TOF-SIMS, TOF.SIMS 5, IONTOF, Germany). The inductively coupled plasma–optical emission spectroscopy (ICP-OES, OPTIMA 8300, PerkinElmer, Inc., United States) exhibited a cationic ratio of all samples.

Temperature-programmed reduction (TPR) was carried out in an AutoChem II 2920 (Protech Korea, South Korea) under 10% H_2 in Ar (total flow rate 50 ml min^{-1}) to compare the oxidizing power of samples under a reducing atmosphere. Gas sensing was performed with 11 different gas species (NO_2, SO_2, H_2S, NH_3, H_2, C_3H_6O, C_6H_6, C_7H_8, CO, P-xylene, and C_2H_5OH).

The Mott–Schottky plot was measured using the electrochemical impedance spectroscopy (EIS) tool (potentiostat, 1287A, Solartron, UK) combined with a frequency analyzer (1260, Solartron, UK). The VBM in *p*-type of $NiWO_4$ and CBM in *n*-type of $Cu_{0.25}Ni_{0.75}WO_4$ and $Li_{0.10}Cu_{0.25}Ni_{0.75}WO_4$ levels are calculated using the equations below. The flat-band potentials (E_{fb}) of all samples were computed to be $NiWO_4$: 2.14 V, $Cu_{0.25}Ni_{0.75}WO_4$: −1.55 V, $Li_{0.10}Cu_{0.25}Ni_{0.75}WO_4$: −1.48 V versus saturated calomel electrode (SCE). The E_{CB} of a *p*-type semiconductor is usually ≈0.1 or 0.2 V more positive than its E_{fb}, while the E_{CB} of an *n*-type semiconductor is typically 0.1 or 0.2 V more negative than the E_{fb}. Using the formula $E_{NHE} = E_{SCE} + X$ (observed value), the E_{VB} of $NiWO_4$ and the E_{CB} of $Cu_{0.25}Ni_{0.75}WO_4$ and $Li_{0.10}Cu_{0.25}Ni_{0.75}WO_4$ were calculated to be 1.61 and −1.51 V, −1.44 V versus normal hydrogen electrode (NHE), respectively.

The DC conductivity and E_a were calculated using Jonscher's power-law from frequency-dependent AC conductivity as the following equation:

$$\sigma_{AC} = \sigma_{DC} + AW^s \tag{1}$$

here, A is a pre-exponential factor depending on temperature frequency, W is the angular frequency, and s is the frequency exponent with values in the range $0 \leq s \leq 1$. The resistivity (ρ) is derived from the reciprocal value of conductivity (σ), and the calculation of E_a is obtained through a linear fit using the following equation:

$$\rho/T = \rho_0 \exp E_a/K_B T \tag{2}$$

Calculation of Electronic Structure: First-principles density functional theory (DFT) calculations were conducted using the projector-augmented-wave (PAW) method[35] and the Perdew–Burke–Ernzerhof (PBE) functional,[36] as implemented in the Vienna Ab initio Simulation Package (VASP). The valence electrons considered were 3d and 4s for Ni, 5d and 6s for W, 2s and 2p for O, 3d and 4s for Cu, and 1s and 2s for Li. To accurately describe electron-electron correlations, on-site Coulomb interactions were incorporated using a simplified rotationally invariant approach.[37] The difference between the Coulomb U and exchange J parameters, $U_{eff} = U - J$, was set to 5.3 eV for the Ni 3d and Cu 3d orbitals.[38,39] The plane-wave basis cut-off energy was set to 800 eV, and a $2a \times 2b \times 2c$ supercell was used to model Cu substitution and interstitial Li incorporation. Structural relaxation was performed until the Hellmann–Feynman forces were below 5×10^{-3} eV $Å^{-1}$. For Cu substitution at the Ni site, 1/8 of the Ni atoms were replaced with Cu, forming $Ni_{7/8}Cu_{1/8}WO_4$. In the case of interstitial Li incorporation, four possible Li sites (two octahedral and two tetrahedral interstitial sites) were considered, with the most stable configuration determined based on total energy minimization.

Supporting Information

Supporting Information is available from the Wiley Online Library or from the author.

Acknowledgements

S.Y.L., H.E.C., and S.J.C. contributed equally to this work. This study was supported by Samsung Electronics Co., Ltd. (IO201216–08204-01). This work was also supported by the National Research Foundation of Korea (NRF) grant funded by the Korean government (MSIT) (No. 2022R1A2C2005210).

Conflict of Interest

The authors declare no conflict of interest.

Data Availability Statement

The data that support the findings of this study are available from the corresponding author upon reasonable request.

Keywords

gas sensor, H_2S, $NiWO_4$, sub-gap band

Received: December 23, 2024
Revised: March 1, 2025
Published online:

[1] Y.-B. Hahn, R. Ahmad, N. Tripath, *Chem. Commun.* **2012**, *48*, 10369.
[2] Y.-F. Sun, S.-B. Liu, F.-L. Meng, J.-Y. Liu, Z. Jin, L.-T. Kong, J.-H. Liu, *Sensors* **2012**, *12*, 2610.
[3] A. Day, *Mater. Sci. Eng. B* **2018**, *229*, 206.
[4] G. Korotcenkov, *Handbook of Gas Sensor Materials: Properties, Advantages and Shortcomings for Applications*, Vol. *1*, Springer, New York, **2013**.
[5] G. Korotcenkov, *Handbook of Gas Sensor Materials: Properties, Advantages and Shortcomings for Applications*, Vol. *2*, Springer, New York, **2014**.
[6] H. Kim, J. Lee, *Sens. Actuators, B* **2014**, *192*, 607.
[7] D. R. Miller, S. A. Akbar, P. A. Morris, *Sens. Actuators, B* **2014**, *204*, 250.
[8] B. Choi, D. Shin, H. Lee, H. Song, *Nanoscale* **2022**, *14*, 338.
[9] Z. Fan, J. G. Lu, *Metal Oxide Nanowires: Fundamentals and Sensor Applications in Metal Oxide Nanomaterials for Chemical Sensors*, Springer, New York, **2013**.
[10] G. Horvai, *Sens. Actuators, B* **1997**, *43*, 94.
[11] P. Ernest, S. Michael, S. Shababa, D. R. James, B. A. Artem, W. Aron, *Nat. Rev. Mater.* **2022**, *7*, 503.
[12] S. Yuanmiao, C. Gao, X. Shibo, J. X. Zhichuan, *ACS Catal.* **2021**, *11*, 13947.
[13] Y. Zhao, S. Zhang, R. Shi, G. I. N. Waterhouse, J. Tang, T. Zhang, *Mater. Today* **2020**, *34*, 78.
[14] S. Nopparat, C. Surawut, L. Navadol, C. Verawat, S. Takashi, *ACS Omega* **2020**, *5*, 20373.
[15] X. Huang, *Res. Chem. Intermed.* **2020**, *46*, 5133.
[16] P. Liu, J. Ran, B. Xia, S. Xi, D. Gao, J. Wang, *Nano-Micro Lett.* **2020**, *12*, 68.
[17] J. Li, E. Na, X. Liang, Q. Liang, M. Fan, H. Chen, G.-D. Li, X. Zou, *Inorg. Chem. Front.* **2024**, *11*, 8602.
[18] E. Na, S. Tao, W. Wang, J. Li, Y. Guo, R. Gao, Q. Li, F. Wang, C. Zhang, G.-D. Li, *ACS Sens.* **2024**, *9*, 6148.
[19] M. Imada, A. Fujimori, Y. Tokura, *Rev. Mod. Phys.* **1998**, *70*, 1039.
[20] Y. Tokura, N. Nagaosa, *Science* **2000**, *288*, 462.
[21] J. Jeong, N. Aetukuri, T. Graf, T. D. Schladt, M. G. Samant, S. S. P. Parkin, *Science* **2013**, *339*, 1402.
[22] E. Dagotto, *Science* **2005**, *309*, 257.
[23] A. Bhargava, R. Eppstein, J. Sun, M. A. Smeaton, H. Paik, L. F. Kourkoutis, D. G. Schlom, M. C. Toroker, R. D. Robinson, *Adv. Mater.* **2020**, *32*, 2004490.
[24] Y. Takashi, N. H. Azusa, N. P. Liliany, T. Shohei, H. Ken, D. Hiroshi, S. Kazunori, T. Hidekazu, *ACS Appl. Electron. Mater.* **2019**, *1*, 2678.
[25] C. Shang, C. Cao, D. Yu, Y. Yan, Y. Lin, H. Li, T. Zheng, X. Yan, W. Yu, S. Zhou, J. Zeng, *Adv. Mater.* **2019**, *31*, 1805104.
[26] P. Watthaisong, S. Jungthawan, P. Hirunsit, S. Suthirakun, *RSC Adv.* **2019**, *9*, 19483.
[27] S. G. Park, K. H. Lee, J.-H. Lee, G. Bang, J. Kim, H. J. Park, M. S. Oh, S. Lee, Y.-H. Kim, Y.-M. Kim, H. Hosono, J. Bang, K. Lee, *Inorg. Chem. Front.* **2020**, *7*, 853.
[28] E. Y. Joseph, J. P. Kayla, B. K. Joshua, M. B. Bart, *J. Phys. Chem. C* **2013**, *117*, 8708.
[29] M. V. Lalić, Z. S. Popović, F. R. Vukajlović, *Comput. Mater. Sci.* **2012**, *63*, 163.
[30] C. M. Tian, M. Jiang, D. Tang, L. Qiao, H. Y. Xiao, F. E. Oropeza, J. P. Hofmann, E. J. M. Hensen, A. Tadich, W. Li, D. C. Qi, K. H. L. Zhang, *J. Mater. Chem. A* **2019**, *7*, 11895.
[31] S. M. M. Zawawi, R. Yahya, A. Hassan, H. N. M. E. Mahmud, M. N. Daud, *Chem. Cent. J.* **2013**, *7*, 80.
[32] S. D. Ramarao, V. R. K. Murthy, *Dalton Trans.* **2015**, *44*, 2311.
[33] Q. Bao, S. Bao, C. M. Li, X. Qi, C. Pan, J. Zang, W. Wang, D. Y. Tang, *Chem. Mater.* **2007**, *19*, 5965.
[34] H. Liu, T. Yan, Z. Jin, Q. Ma, *New J. Chem.* **2020**, *44*, 1426.
[35] P. E. Blöchl, *Phys. Rev. B* **1994**, *50*, 17953.
[36] J. P. Perdew, K. Burke, M. Ernzerhof, *Phys. Rev. Lett.* **1996**, *77*, 3865.
[37] G. Kresse, J. Furthmüller, *Phys. Rev. B* **1996**, *54*, 11169.
[38] S. L. Dudarev, G. A. Botton, S. Y. Savrasov, C. J. Humphreys, A. P. Sutton, *Phys. Rev. B* **1998**, *57*, 1505.
[39] H. Chen, J. H. Harding, *Phys. Rev. B* **2012**, *85*, 115127.